Dynamic Forces between Bubbles and Surfaces and Hydrodynamic Boundary Conditions

Ofer Manor,[†] Ivan U. Vakarelski,[†,||] Geoffrey W. Stevens,[†] Franz Grieser,[†] Raymond R. Dagastine,[†] and Derek Y. C. Chan*[,†,‡,§]

Particulate Fluids Processing Centre, University of Melbourne, Parkville, Victoria 3010, Australia, Department of Mathematics, National University of Singapore, 117543 Singapore, Institute of High Performance Computing, 1 Science Park Road, 117528 Singapore, and Institute of Chemical and Engineering Sciences, 1 Pesek Road, Jurong Island, 627833 Singapore

Received July 10, 2008. Revised Manuscript Received August 16, 2008

A bubble attached to the end of an atomic force microscope cantilever and driven toward or away from a flat mica surface across an aqueous film is used to characterize the dynamic force that arises from hydrodynamic drainage and electrical double layer interactions across the nanometer thick intervening aqueous film. The hydrodynamic response of the air/water interface can range from a classical fully immobile, no-slip surface in the presence of added surfactants to a partially mobile interface in an electrolyte solution without added surfactants. A model that includes the convection and diffusion of trace surface contaminants can account for the observed behavior presented. This model predicts quantitatively different interfacial dynamics to the Navier slip model that can also be used to fit dynamic force data with a *post hoc* choice of a slip length.

1. Introduction

Hydrodynamic boundary conditions on the nanometer length scale and their effects on dynamic forces involving deformable bodies underpin developments in micro- and nanofluidic engineering applications[1] and in biomedical modeling.[2] Interactions involving micrometer-sized bubbles are also of particular interest because of their role as a contrast agent in ultrasonic diagnostic applications and as drug delivery vectors.[3] Numerous theoretical studies explored the nature of hydrodynamic boundary conditions in single phase flow near simple solid surfaces[4−7] to quantify the Navier boundary slip model where the ratio of the fluid velocity to the tangential velocity gradient at the surface is given by a slip length. Measurements of the hydrodynamic force between two molecularly smooth mica sheets across wetting liquids down to sub-nanometer separations indicate that the no-slip boundary condition (zero slip length) applies for such systems.[8−12] Direct observations[13,14] and modeling[15−17] of time dependent drainage and deformations of sub-nanometer thick aqueous films between a deformable mercury drop and an approaching and receding mica plate also indicate the applicability of the no-slip boundary condition at the water/mica and water/mercury interfaces. However, a recent study[18] reported slip lengths of up to 20 nm using a similar apparatus, although the deduced slip length can vary by 1 order of magnitude depending on the method of data analysis. Dynamic force measurements using the atomic force microscope (AFM) with micrometer-sized particles reported evidence of hydrodynamic slip at wetted surfaces,[19−23] although a recent AFM study of hydrodynamic forces between hydrophilic (wetted) particles concluded that the slip length in such systems is zero within an experimental uncertainty of ±1 nm.[24] AFM measurements of hydrodynamic forces between deformable decane and tetradecane drops stabilized by surfactants in water[25−29] and also between such oil drops and solid particles[30]

* To whom correspondence should be addressed. E-mail: D.Chan@unimelb.edu.au.
[†] University of Melbourne.
[‡] National University of Singapore.
[§] Institute of High Performance Computing.
[||] Institute of Chemical and Engineering Sciences.

(1) Whitesides, G. M. *Nature* **2006**, *442*, 368.
(2) Taylor, C. A.; Draney, M. T. *Annu. Rev. Fluid Mech.* **2004**, *36*, 197–231.
(3) Lohse, D. *Phys. Today* **2003**, *56*(2), 36–41.
(4) Barrat, J. L.; Bocquet, L. *Phys. Rev. Lett.* **1999**, *82*(23), 4671–4674.
(5) Cieplak, M.; Koplik, J.; Banavar, J. R. *Phys. Rev. Lett.* **2001**, *86*(5), 803–806.
(6) Thompson, P. A.; Robbins, M. O. *Phys. Rev. A: At., Mol., Opt. Phys.* **1990**, *41*(12), 6830–6837.
(7) Thompson, P. A.; Troian, S. M. *Nature* **1997**, *389*(6649), 360–362.
(8) Chan, D. Y. C.; Horn, R. G. *J. Chem. Phys.* **1985**, *83*(10), 5311–24.
(9) Cottin-Bizonne, C.; Cross, B.; Steinberger, A.; Charlaix, E. *Phys. Rev. Lett.* **2005**, *94*(5),
(10) Cottin-Bizonne, C.; Jurine, S.; Baudry, J.; Crassous, J.; Restagno, F.; Charlaix, E. *Eur. Phys. J. E* **2002**, *9*(1), 47–53.
(11) Horn, R. G.; Smith, D. T.; Haller, W. *Chem. Phys. Lett.* **1989**, *162*(4−5), 404–408.
(12) Israelachvili, J. N. *J. Colloid Interface Sci.* **1986**, *110*(1), 263–271.
(13) Connor, J. N.; Horn, R. G. *Faraday Discuss.* **2003**, *123*, 193–206.
(14) Clasohm, L. Y.; Connor, J. N.; Vinogradova, O. I.; Horn, R. G. *Langmuir* **2005**, *21*(18), 8243–8249.
(15) Manica, R.; Connor, J. N.; Carnie, S. L.; Horn, R. G.; Chan, D. Y. C. *Langmuir* **2007**, *23*(2), 626–637.
(16) Manica, R.; Connor, J. N.; Clasohm, L. Y.; Carnie, S. L.; Horn, R. G.; Chan, D. Y. C. *Langmuir* **2008**, *24*(4), 1381–1390.
(17) Manica, R.; Connor, J. N.; Dagastine, R. R.; Carnie, S. L.; Horn, R. G.; Chan, D. Y. C. *Phys. Fluids* **2008**, *20*(3), 032101.
(18) Cottin-Bizonne, C.; Steinberger, A.; Cross, B.; Raccurt, O.; Charlaix, E. *Langmuir* **2008**, *24*(4), 1165–1172.
(19) Bonaccurso, E.; Butt, H.-J.; Craig, V. S. J. *Phys. Rev. Lett.* **2003**, *90*(14), 144501/1–144501/4.
(20) Bonaccurso, E.; Kappl, M.; Butt, H.-J. *Phys. Rev. Lett.* **2002**, *88*(7), 076103/1–076103/4.
(21) Neto, C.; Craig, V. S. J.; Williams, D. R. M. *Eur. Phys. J. E* **2003**, *12*(Suppl. 1), S71–S74.
(22) Neto, C.; Evans, D. R.; Bonaccurso, E.; Butt, H.-J.; Craig, V. S. J. *Rep. Prog. Phys.* **2005**, *68*(12), 2859–2897.
(23) Pit, R.; Hervet, H.; Leger, L. *Phys. Rev. Lett.* **2000**, *85*(5), 980–983.
(24) Honig, C. D. F.; Ducker, W. A. *Phys. Rev. Lett.* **2007**, *98*(2),
(25) Carnie, S. L.; Chan, D. Y. C.; Lewis, C.; Manica, R.; Dagastine, R. R. *Langmuir* **2005**, *21*(7), 2912–2922.
(26) Dagastine, R. R.; Chau, T. T.; Chan, D. Y. C.; Stevens, G. W.; Grieser, F. *Faraday Discuss.* **2005**, *129*, 111–124.
(27) Dagastine, R. R.; Manica, R.; Carnie, S. L.; Chan, D. Y. C.; Stevens, G. W.; Grieser, F. *Science (Washington, DC)* **2006**, *313*(5784), 210–213.
(28) Dagastine, R. R.; Stevens, G. W.; Chan, D. Y. C.; Grieser, F. *J. Colloid Interface Sci.* **2004**, *273*(1), 339–342.
(29) Webber, G. B.; Edwards, S. A.; Stevens, G. W.; Grieser, F.; Dagastine, R. R.; Chan, D. Y. C. *Soft Matter* **2008**, *4*, 1270–1278.
(30) Webber, G. B.; Manica, R.; Edwards, S. A.; Carnie, S. L.; Stevens, G. W.; Grieser, F.; Dagastine, R. R.; Chan, D. Y. C. *J. Phys. Chem. C* **2008**, *112*(2), 567–574.

10.1021/la802206q CCC: $40.75 © 2008 American Chemical Society
Published on Web 09/23/2008

all indicate that a no-slip hydrodynamic boundary condition applies at the oil/water interface in the presence of surfactants. Recent studies of the drainage dynamics of micrometer thick silicone oil films between approaching millimeter size glycerol drops[31] and of the dynamic response of a film of glycerol−water mixture between a millimeter particle and a bubble raft also indicate the applicability of the no-slip boundary condition at the fluid/fluid interface and at the bubble/fluid interface.[32]

Here, we report AFM measurements of dynamic forces acting on a bubble (∼50 μm radius) anchored at the end of a custom-made cantilever that is driven toward or separated from a molecularly smooth mica plate in a controlled manner in a simple electrolyte and in the presence of surfactants. Electrical double layer repulsion between the bubble and the mica across aqueous films down to ∼30 nm thick together with hydrodynamic interactions cause the bubble to deform during interaction. By modeling variations of the force with time during both the approach and retraction of the bubble from the mica surface, we can determine the hydrodynamic boundary condition that must hold at the air/water interface: the simplest smooth and deformable interface whose interfacial properties can be controlled by the addition of surfactants. Preliminary results have been presented elsewhere.[33]

Details of bubble-surface experimental force measurements in water are presented in section 2. Theoretical models are developed in section 3, where we considered different boundary conditions at the air/water interface including the no-slip boundary condition (or tangentially immobile interface), the full-slip boundary condition (or the fully mobile interface with no tangential stress), the Navier slip boundary condition in which the ratio of the surface velocity to the derivative of the surface velocity in the direction normal to the interface is a constant called the slip length, and a model that incorporates the effects of surface diffusion and convection of a small amount of insoluble surfactants or impurities at the air/water interface. Measured dynamic forces are compared with theory in section 4, and predictions of the different models are contrasted in section 5. The paper closes with a conclusion.

2. Experiments

We employed ultrasound to generate large populations of bubbles in the size range from several tens to several hundred micrometers on a weakly hydrophobic surface.[34] A bubble of ∼50 μm radius was then picked up and anchored to a hydrophobized circular gold patch of 40 μm diameter (thickness 20 nm) that was centered at 5 μm from the end of a custom-manufactured rectangular silicon AFM cantilever of dimensions 450 μm × 50 μm × 3 μm[35] (Figure 1). The spring constant of the cantilever K was determined by the Cleveland method.[36] The dynamic force between such a bubble and a freshly cleaved mica plate was first measured in distilled water with 1 mM $NaNO_3$ electrolyte. With the bubble remaining on the cantilever, the electrolyte was then exchanged for a 10 mM sodium dodecyl sulfate (SDS) solution that resulted in a monolayer of SDS being adsorbed at the surface of the bubble. The dynamic force between this surfactant coated bubble and the mica was then measured in the presence of the SDS solution.

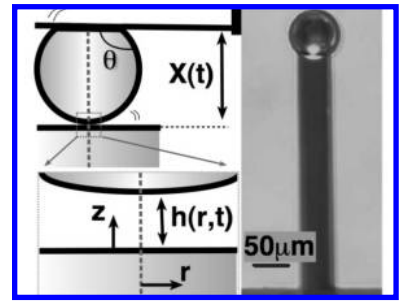

Figure 1. Schematic diagram of the AFM with the coordinate system and a photograph of a bubble on the rectangular cantilever

SDS did not adsorb significantly onto the mica, as it was negatively charged. During the course of the entire experiment in electrolyte and in SDS solution, which lasts for 20−30 min, the bubble shrank in size by about 10% due to slow gas dissolution. The bubble size was monitored at the beginning and end of each force measurement to confirm that the bubble size did not change significantly. The experiments were carried out on an Asylum MFP-3D AFM equipped with a linear variable differential transformer (LVDT) which reports the actual location $X(t)$ of the z-piezo as it moves through the approach/retract cycle of a force−displacement measurement with $t = 0$ being the start of the approach/retract cycle. From Figure 2a, we see that, for a nominal scan rate setting of the piezo drive, which corresponds to a nominal average piezo drive velocity, the LVDT piezo position $X(t)$ does not vary linearly with time but has time varying instantaneous velocities $V(t) = dX(t)/dt$ as shown in Figure 2b. This suggests that a more fundamental way to present and analyze our experiments is to consider time variations of the cantilever deflection that can be converted to force via the cantilever spring constant.

3. Theory

The dynamic force $F(t)$ can be modeled by an axisymmetric model (Figure 1) that couples the thickness $h(r,t)$ of the water film between the mica and the deforming bubble, the hydrodynamic pressure $p(r,t)$, and the disjoining pressure $\Pi(h(r,t))$ in the aqueous film due to electrical double layer interactions calculated using the nonlinear Poisson−Boltzmann theory.[37] van der Waals interactions are negligible in the range of film thicknesses in the present system. With a constant air/water interfacial tension σ and a Newtonian viscosity μ to characterize the aqueous film, the equations that govern film deformation and film thinning are as follows:[25,38]

$$\frac{\sigma}{r}\frac{\partial}{\partial r}\left[r\frac{\partial h}{\partial r}\right] = \Delta P - (p + \Pi) \tag{1}$$

$$\frac{\partial h}{\partial t} = -\frac{1}{r}\frac{\partial}{\partial r}[rQ] \tag{2a}$$

$$\mu\frac{\partial^2 u}{\partial z^2} = \frac{\partial p}{\partial r} \tag{2b}$$

$$F(t) = 2\pi\int_0^\infty [p(r,t) + \prod(h(r,t))]r\,dr \tag{3}$$

Equation 1 is the augmented Young−Laplace equation that describes variations of the thickness of an aqueous film $h(r,t)$ between the mica and the air/water interface of the bubble. This equation is derived by balancing the normal stress with the local curvature of the air/water interface of the bubble while assuming a constant surface tension.[17] As deformations are small compared to the undeformed bubble radius R_b, the Laplace pressure ΔP

(31) Manica, R.; Klaseboer, E.; Chan, D. Y. C. *Soft Matter* **2008**, *4*, 1613–1616.
(32) Steinberger, A.; Cottin-Bizonne, C.; Kleimann, P.; Charlaix, E. *Phys. Rev. Lett.* **2008**, *100*, 134501.
(33) Manor, O.; Vakarelski, I. U.; Tang, X.; O'Shea, S. J.; Stevens, G. W.; Grieser, F.; Dagastine, R.; Chan, D. Y. C. *Phys. Rev. Lett.* **2008**, *101*, 024501.
(34) Vakarelski, I. U.; Lee, J.; Dagastine, R. R.; Chan, D. Y. C.; Stevens, G. W.; Grieser, F. *Langmuir* **2008**, *24*(3), 603–605.
(35) Manor, O.; Vakarelski, I. U.; Tang, X.; O'Shea, S. J.; Stevens, G. W.; Grieser, F.; Dagastine, R. R.; Chan, D. Y. C. *Phys. Rev. Lett.* **2008**, *101*, 024501.
(36) Cleveland, J. P.; Manne, S.; Bocek, D.; Hansma, P. K. *Rev. Sci. Instrum.* **1993**, *64*(2), 403–405.
(37) McCormack, D.; Carnie, S. L.; Chan, D. Y. C. *J. Colloid Interface Sci.* **1995**, *169*(1), 177–196.
(38) Manica, R.; Connor, J. N.; Dagastine, R. R.; Carnie, S. L.; Horn, R. G.; Chan, D. Y. C. *Phys. Fluids* **2008**, *20*, 032101.

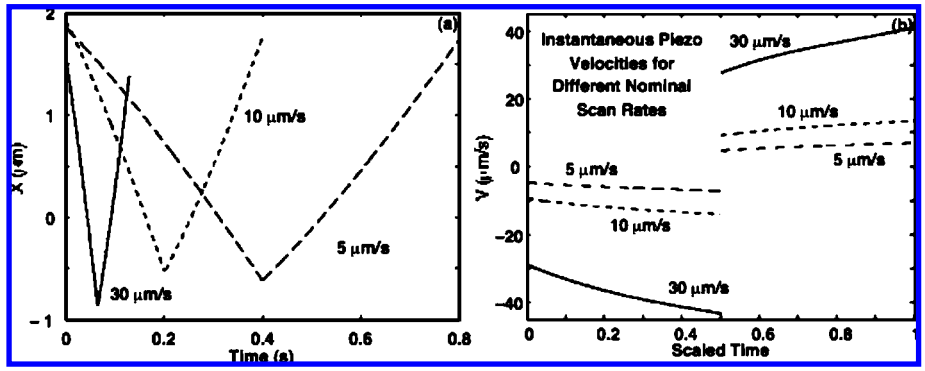

Figure 2. Time variations of the LVDT output: (a) the relative displacement of the AFM cantilever, $X(t)$ (z-piezo), and (b) the instantaneous velocity, $V(t) = \mathrm{d}X(t)/\mathrm{d}t$, at different nominal scan rates calculated by differentiation of fourth order polynomials fitted separately to the approach and retract branches. The time axis in (b) is scaled by the period of an approach−retract cycle. A decrease in $X(t)$ corresponds to a decrease in the gap between the cantilever and the mica surface.

can be approximated by $(2\sigma/R_b)$.[17] The thinning or thickening of the aqueous film as a bubble approaches or retracts from the mica is governed by eq 2, which follows from the Reynolds lubrication theory for the dominant radial component of the fluid velocity $u(z,t)$, with $Q(r,t) \equiv \int_0^{h(r,t)} u(z,t)\,\mathrm{d}z$. Equations 1 and 2 are to be solved in the inner region $0 < r < r_{max}$. Detailed scaling arguments for the choice of r_{max} are given elsewhere,[17,25] but for a 50 μm bubble $r_{max} \sim 15$ μm is sufficient for numerical convergence. The boundary conditions for different quantities at $r = 0$ are governed by symmetry considerations. The outer boundary condition for the thickness h of the film at r_{max} follows from volume conservation of the bubble and obeys the constraint that the base of the bubble is anchored to the cantilever. This condition takes the form:[17,25]

$$\frac{\mathrm{d}X}{\mathrm{d}t} = \frac{\partial h}{\partial t} + \frac{\alpha}{2\pi\sigma}\frac{\mathrm{d}F}{\mathrm{d}t} \quad \text{at} \quad r = r_{max} \tag{4a}$$

$$\alpha = \log_e\left(\frac{r_{max}}{R_b}\right) + 1 + \frac{1}{2}\log_e\left(\frac{1+\cos(\theta)}{1-\cos(\theta)}\right) - \frac{2\pi\sigma}{K} \tag{4b}$$

where θ is the contact angle of the bubble at the cantilever. An additional boundary condition for the hydrodynamic pressure at $r = r_{max}$ will be discussed in the next subsections. The function $X(t)$ is taken from the raw LVDT data, and $\mathrm{d}X/\mathrm{d}t$ is calculated by differentiating a fourth order polynomial fitted to approximately 2000 experimental data points for variations of the location of the AFM's cantilever with time (Figure 2). The initial condition for the film thickness is $h(r,0) = h_{init} + r^2/(2R_b)$, which corresponds to an undeformed bubble. The initial distance of closest approach h_{init} between the bubble and the mica cannot be determined experimentally but can be estimated by fitting to the initial part of the force curve before bubble deformation becomes significant.[17] Finally, two boundary conditions are required to solve eq 2b. At the mica/water interface ($z = 0$), we assumed the no-slip or fully immobile boundary condition, which corresponds to $u = 0$ at $z = 0$ (Figure 1). Different options for the boundary condition at the air/water interface ($z = h$), which represent different physical phenomena, will be discussed in the next subsections.

3.1. No-Slip Boundary Condition at the Air/Water Interface. It is well-known that the presence of a layer of surfactants interferes with the tangential flow at an interface and can immobilize it.[39] The appropriate boundary condition at such an interface is the no-slip boundary condition (such a surface is also referred to as a fully immobile interface), which in the present system it is implemented in the form: $u = 0$ at $z = h$.[17,40] Equation 2, subject to the no-slip boundary condition at the surfaces of the mica and the bubble, becomes

$$\frac{\partial h}{\partial t} = \frac{1}{12\mu r}\frac{\partial}{\partial r}\left(rh^3\frac{\partial p}{\partial r}\right) \tag{5}$$

The additional outer boundary condition for the hydrodynamic pressure is the asymptotic decay, $p \sim c/r^4$ for $r \geq r_{max}$, according to an asymptotic analysis of eq 5.[17] This condition can be written as $\partial p/\partial r + (4/r)p = 0$ at r_{max}, which eliminates the unknown constant c.

3.2. Full-Slip Boundary Condition at the Air/Water Interface. At an ideal clean interface, the tangential stress must be continuous, and the vanishing small viscosity in the bubble implies that the tangential stress must vanish at an ideal clean air/water interface. This gives rise to the full-slip boundary condition described by $\partial u/\partial z = 0$ at the air/water interface ($z = h$). Equation 2 subject to a no-slip boundary condition at the mica and a full-slip boundary condition at the bubble becomes

$$\frac{\partial h}{\partial t} = \frac{1}{3\mu r}\frac{\partial}{\partial r}\left(rh^3\frac{\partial p}{\partial r}\right) \tag{6a}$$

which only differs from eq 5 by a factor of 4 because the radial flow rate Q in eq 2 is increased by the same factor as a result of lower hydrodynamic resistance arising from the full-slip condition at the bubble surface. The tangential velocity of the air/water interface is

$$u(z = h, r, t) = u_s = -\left(\frac{h^2}{2\mu}\right)\left(\frac{\partial p}{\partial r}\right) \tag{6b}$$

The outer boundary condition for the pressure is unchanged: $\partial p/\partial r + (4/r)p = 0$ at r_{max}, as the qualitative decay of the hydrodynamic pressure is indifferent to the degree of mobility of the air/water interface.

3.3. Navier Slip Boundary Condition at the Air/Water Interface. Variations of the air/water interface mobility between the two limits mentioned in the previous two subsections can be modeled by the Navier slip model characterized by a slip length b (ref 41), which is a constant of proportionality between the velocity and its tangential derivative at the interface: $u = -b(\partial u/\partial z)$ at $z = h$. For a

(39) Levich, V. G. *Physicochemical hydrodynamics*; Prentice Hall: Englewood Cliffs, NJ, 1962.

(40) Carnie, S. L.; Chan, D. Y. C.; Gunning, J. S. *Langmuir* **1994**, *10*(9), 2993–3009.

Newtonian fluid, the tangential derivative is proportional to the shear stress. With this model, eq 2 becomes

$$\frac{\partial h}{\partial t} = \frac{1}{12\mu r}\frac{\partial}{\partial r}\left[rh^3\frac{\partial p}{\partial r}\left(\frac{4b+h}{b+h}\right)\right] \tag{7a}$$

and the tangential velocity at the air/water interface has the form

$$u(z=h,r,t) = u_s = -\left(\frac{h^2}{2\mu}\right)\left(\frac{b}{b+h}\right)\left(\frac{\partial p}{\partial r}\right) \tag{7b}$$

The slip length, b, is an unknown adjustable parameter. The outer boundary condition for the pressure is unchanged: $\partial p/\partial r + (4/r)p = 0$ at r_{max}.

3.4. Insoluble Surface Impurities at the Air/Water Interface. We develop a model to quantify the effects on the hydrodynamic boundary condition[39] due to the inevitable presence of trace impurities at the air/water interface. The presence of a low surface concentration Γ of insoluble surface-active impurity at the air/water interface depresses the interfacial tension from the ideal value σ_0 to a lower value: $\sigma = \sigma_0 - \pi_s$ by the surface pressure π_s of the surface impurities. Variations in π_s along the interface produces the tangential stress boundary condition for eq 2b: $\mu\partial u/\partial z = -\partial\pi_s/\partial r$ at the air/water interface ($z = h$) according to the simple Marangoni type model developed by Levich.[39] As a result, the film thinning equation, eq 2, becomes

$$\frac{\partial h}{\partial t} = \frac{1}{3\mu r}\frac{\partial}{\partial r}\left(rh^3\frac{\partial p}{\partial r}\right) + \frac{1}{2\mu r}\frac{\partial}{\partial r}\left(rh^2\frac{\partial \pi_s}{\partial r}\right) \tag{8a}$$

and the tangential velocity at the air/water interface is

$$u(z=h,r,t) = u_s = -\left(\frac{h^2}{2\mu}\right)\left(\frac{\partial p}{\partial r}\right) - \left(\frac{h}{\mu}\right)\left(\frac{\partial \pi_s}{\partial r}\right) \tag{8b}$$

The surface-active impurity is assumed to remain at the air/water interface and does not transfer into the aqueous phase during interaction. The two-dimensional ideal gas equation $\pi_s = k_B T\,\Gamma(r,t)$ (where k_B and T are the Boltzmann constant and the temperature, respectively) is used to relate the surface pressure and the low surface concentration of impurities. Under these assumptions the surface convection−diffusion equation that specifies material conservation along the interface is

$$\frac{\partial \pi_s}{\partial t} + \nabla_t\cdot[(u_s\hat{r})\pi_s] = D\nabla_t^2\pi_s \tag{9}$$

where D is the diffusion coefficient, $(u_s\hat{r})$ is the tangential velocity at the air/water interface, and the operator ∇_t depends only on the radial coordinate r tangential to the interface.[42] The relative importance of convective to diffusive effects in eq 9 is measured by the Peclet number, $Pe = \lambda^2/D\tau$, where λ is a characteristic length in the radial direction and τ is a characteristic time. In terms of the capillary number $Ca = \mu V/\sigma$, our governing equations are scaled as follows:[25] in the radial dimension $r^* = R_b Ca^{1/4}$ and in time $t^* = Ca^{-1/2}(R_b\mu/\sigma)$. With $D \sim 10^{-9}$ m^2/s, the magnitude of $Pe \sim r^{*2}/Dt^* \sim R_bV/D \sim 1$ suggests that all three terms in the convection−diffusion equation, eq 9, are of comparable magnitude. We specify the concentration of surface-active impurity by assuming an initial quiescent value for the surface pressure $\pi_{s0} = \sigma_0 - \sigma_{init}$, that is, within uncertainties in determining interfacial tensions. The surface pressure is scaled by $\pi_s^* = \sigma_{init}Ca^{1/2}$. As the experimental time scale is short (~0.1 s) compared to the diffusion time over the extent of the bubble (~$R_b^2/D \sim 2$ s), the bubble interfacial tension outside the interaction zone can be assumed to remain at its equilibrium value during the course of the interaction. Thus, on the scale of interaction zone, $\pi_s \to \pi_{s0}$ as $r \to \infty$. Asymptotic analysis of the film thinning equations then yields the boundary condition $r(\partial\pi_s/\partial r) + 2(\pi_s - \pi_{s0}) = 0$ at $r = r_{max}$ (see the Supporting Information), which enables eqs 1, 3, 8, and 9 to be solved. Note that a slight deviation of the surface tension from its constant value results in small variations in the curvature of the interface of $O[(\partial\pi_s/\partial r)/\sigma]$ that can be neglected to leading order (see the Supporting Information).

Table 1. System Parameters in 1 mM $NaNO_3$ and in 10 mM SDS

parameter	experimental	model
viscosity μ	10^{-3} Pa s	10^{-3} Pa s
spring constant K	90 ± 10 mN/m	80 mN/m
mica surface potential ($NaNO_3$)[43]	−95 ± 10 mV	−90 mV
mica surface potential (SDS)[43]	−75 ± 10 mV	−70 mV
bubble surface potential ($NaNO_3$)[44]	−30 ± 10 mV	−35 mV
bubble surface potential (SDS)[45]	−60 ± 10 mV	−65 mV
interfacial tension σ ($NaNO_3$)	72 ± 1 mN/m	73 mN/m
interfacial tension σ (SDS)	39 ± 1 mN/m	39 mN/m
bubble radius R_b ($NaNO_3$)	55 ± 2 μm	56 μm
bubble radius R_b (SDS)	50 ± 3 μm	47 μm
contact angle θ ($NaNO_3$)	150 ± 5°	152°
contact angle θ (SDS)	147 ± 5°	142°

4. Comparisons between Experiment and Theory

We now present variations of measured dynamic forces between a bubble and a mica surface at varying scan rates in electrolyte solution and in the presence of added surfactant (SDS). The experimental results are compared to predictions by various models that correspond to different hydrodynamic boundary conditions at the air/water interface. Values of input parameters to the models that were either taken from the literature or measured independently are summarized in Table 1 together with their experimental tolerance. The only parameter in the model that is not measurable directly is the initial bubble−mica separation h_{init}. We determine its value by fitting to the initial portion of the force curve before bubble deformation becomes significant. We first consider results in the presence of SDS before we discuss results in pure electrolyte.

Time variations of dynamic force curves obtained in the presence of 10 mM SDS, which is above its critical micelle concentration of 7 mM, are shown in Figure 3 for scan rates between 5 and 30 μm/s. These are compared to the model in section 3.1 where a no-slip boundary condition is applied at the surfactant populated air/water interface of the bubble. In all theoretical results in this paper, the LVDT displacement function $X(t)$ at the corresponding nominal scan rate is used as an input in the calculations. We see very good agreement between experiment and theory, which supports the notion that the bubble surface has been rendered immobile by adsorbed SDS and the no-slip hydrodynamic boundary condition applies.

In electrolyte (no surfactant), we see in Figure 4 that the experimental results at the highest scan rate of 30 μm/s lie between the two extreme limits of the no-slip boundary condition (section 3.1) and the full-slip boundary condition (section 3.2) at the bubble surface. The comparisons at lower scan rates are similar.

The mobility of the air/water interface between the no-slip and full-slip limits mentioned above can be varied using the

(41) Vinogradova, O. I. *Langmuir* **1996**, *12*(24), 5963–5968.
(42) Chesters, A. K.; Bazhlekov, I. B. *J. Colloid Interface Sci.* **2000**, *230*, 229–243.
(43) Scales, P. J.; Grieser, F.; Healy, T. W. *Langmuir* **1990**, *6*(3), 582–589.
(44) Takahashi, M. *J. Phys. Chem. B* **2005**, *109*(46), 21858–21864.
(45) Kim, J. Y.; Song, M. G. *J. Colloid Interface Sci.* **2000**, *223*(2), 285–291.
(46) Solomentsev, Y.; White, L. R. *J. Colloid Interface Sci.* **1999**, *218*(1), 122–136.

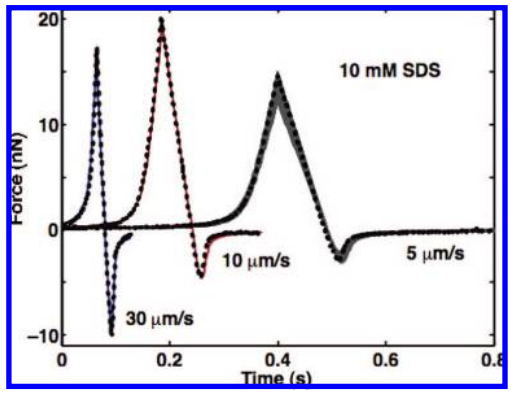

Figure 3. Time variations of the dynamic force $F(t)$ between a bubble and a mica plate in 10 mM SDS at different AFM scan rates. Experimental results (• • •) are samples from over 2000 data points per curve and are compared against the model that applies the no-slip boundary condition at both the mica and bubble surface (—). The initial separations h_{init} are as follows: 2.05 μm (5 μm/s), 1.80 μm (10 μm/s), and 1.87 μm (30 μm/s). The range of possible variations in the predicted force due to uncertainties in experimental input parameters is indicated by the gray line.

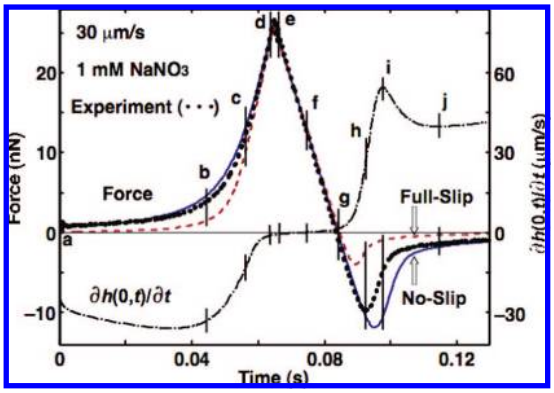

Figure 4. Left axis: Time variations of the dynamic force $F(t)$ between a bubble and a mica plate in distilled water with 1 mM $NaNO_3$ electrolyte at a scan rate of 30 μm/s. The experimental force (• • •) falls between predictions using the no-slip (—) and full-slip (— — —) boundary condition at the air/water interface. The initial separation h_{init} is 1.87 μm. Right axis: The rate of change of the film thickness at the center of the film $r = 0$: $\partial h(0,t)/\partial t$ (— • —) for the insoluble surface impurities model. The times indicated by vertical marks at (a) 0 s, (b) 0.0453 s, (c) 0.0572 s, (d) 0.0646 s, (e) 0.0658 s, (f) 0.0746 s, (g) 0.0840 s, (h) 0.0925 s, (i) 0.0976 s, and (j) 0.115s are referenced in the text.

phenomenological Navier slip model (section 3.3). The theoretical results in Figure 5a for a scan rate of 30 μm/s indicate that a slip length less than 10 nm is close to no-slip (zero slip length) and a slip length greater than 1000 nm will correspond to full-slip (infinite slip length), while a slip length of 17 nm gave good agreement between theory and experiments for all scan rates (see Figure 5b).

While the Navier slip model can be adjusted to fit the bubble−mica dynamic force, it offers no insight into the physical origin of the required slip length of 17 nm. We propose that in electrolyte there remains a small concentration of insoluble surface impurities at the air/water interface that can be convected along the interface by hydrodynamic flow and can themselves undergo surface diffusion. This is the essence of the model presented in section 3.4. For our model, we assume a diffusion coefficient of typical magnitude $D = 10^{-9}$ m^2/s and at a concentration that lowers the ideal air/water interfacial tension by $\pi_{s0} = 0.1$ mN/m. This corresponds to an average surface density of one impurity molecule per 40 nm^2 in a two-dimensional ideal gas. This insoluble surface impurities model also fits the experimental dynamic force results well for all scan rates (Figure 6a). Thus, the present dynamic force measurements indicate the hydrodynamic boundary condition at the air/water interface with 1 mM electrolyte is intermediate between the limits of no-slip and full-slip, and this can be attributed to surface convection and diffusion of insoluble species.

In Figure 6b, we illustrate the effects of changing the equilibrium surface pressure π_{s0} on the dynamic force at a scan rate of 30 μm/s. We see that at surface pressure $\pi_{s0} = 1$ mN/m the interface would effectively behave like a no-slip surface while $\pi_{s0} = 0$ would correspond to a full-slip surface. In addition, the dynamic force is not particularly sensitive to the precise value of the diffusion coefficient as order of magnitude variations over the physical range 10^{-9}−10^{-11} m^2/s for surfactants are needed to produce significant changes in the dynamic force (Figure 7).

5. Dynamics of Different Models

At low scan rates (≤ 1 μm/s), the bubble−surface interaction will be dictated by equilibrium forces and be independent of hydrodynamic boundary conditions. As the scan velocity increases, the precise nature of the hydrodynamic boundary condition becomes more important as dynamic effects progressively dominate. We therefore compare the dynamical behavior of different models at the high scan rate of 30 μm/s. In predicting the dynamic force, the Navier slip model and the insoluble surface impurities model are intermediate between the no-slip and the full-slip models. While conceptually the Navier slip model may be simpler than the insoluble surface impurities model, the value of the slip length is a fitting parameter that cannot be predicted *a priori*. On the other hand the insoluble surface impurities model offers a quantifiable physical model that relates the hydrodynamic boundary condition to the convection and diffusion of surface species. As we shall see, there are other further differences between these models. For all our comparisons hereafter, we use the experimental LVDT displacement function $X(t)$ that corresponds to a nominal rate of 30 μm/s and the initial separation h_{init} is taken to be 1.85 μm.

In Figure 8, the thickness $h(r,t)$ of the aqueous film between the bubble and the mica is shown at the key times marked on the force curve in Figure 4. As a result of the deformability of the air/water interface of the bubble, the minimum film thickness is determined by the balance of repulsive hydrodynamic drainage forces and repulsive electrical double layer interactions between the bubble and the mica and against the Laplace pressure of the bubble (see later discussion around Figures 10 and 11). This predicted minimum film thickness is around 25 nm in all models. The results in Figure 8 also show that, at the deep attractive force minimum, time point (h), the minimum film thickness exceeds 100 nm in all models. At such separations, this attraction is entirely of hydrodynamic origin, as the repulsive disjoining pressure will be negligible. Hydrodynamic dimpling is not predicted in these experiments because the total displacement of the bubble into the mica surface is relatively small as dimpling at high scan rates is only expected when the bubble has been pushed toward the mica far enough beyond the point where the bubble would have contacted the mica had it not deformed.

In qualitative terms, the film thickness of the no-slip, the Navier slip, and the insoluble surface impurities model evolve at a similar rate while the full-slip model approaches and retracts the fastest and the bubble also deforms the most. These observations can be quantified by comparing the normal velocity dh/dt of the bubble surface for different models (Figure 9). In particular, the normal velocity for the full-slip model slows down most rapidly

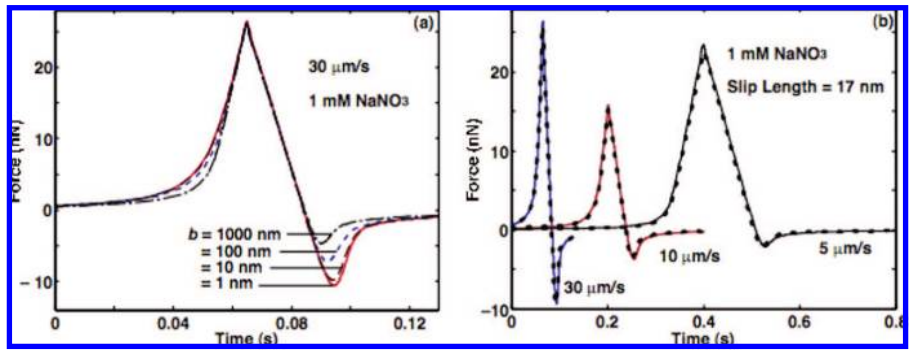

Figure 5. Time variations of the dynamic force $F(t)$ between a bubble and a mica plate in distilled water, with 1 mM NaNO3 according to the Navier slip model: (a) with slip lengths $b = 1$ nm (—) (indistinguishable from no-slip), 10 nm (− − −), 100 nm (- - -), and 1000 nm (− • −) (indistinguishable from full-slip) at the water/mica interface at a scan rate at 30 μm/s; (b) comparison with experimental results (• • •) with the best-fit slip length of 17 nm at the air/water interface (—). The initial separations h_{init} are 1.96 μm (5 μm/s), 2.11 μm (10 μm/s), and 1.85 μm (30 μm/s).

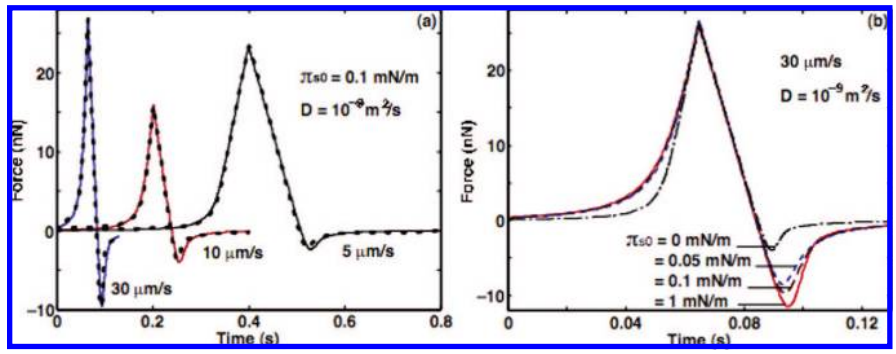

Figure 6. Time variations of the dynamic force $F(t)$ between a bubble and a mica plate in distilled water with 1 mM $NaNO_3$ according to the insoluble surface impurities model with a diffusion coefficient of $D = 10^{-9}$ (a) with the initial magnitude of surface pressure $\pi_{s0} = 0.1$ mN/m (—) compared to experimental results (• • •). The initial separations h_{init} are 1.96 μm (5 μm/s), 2.11 μm (10 μm/s), and 1.85 μm (30 μm/s). (b) Time variations of theoretical dynamic force results with the initial magnitudes of surface pressure $\pi_{s0} = 0$ mN/m (− • −) (same as full-slip), 0.05 mN/m (- - -), 0.1 mN/m (− − −), and 1 mN/m (—) (same as no-slip) at a scan rate of 30 μm/s.

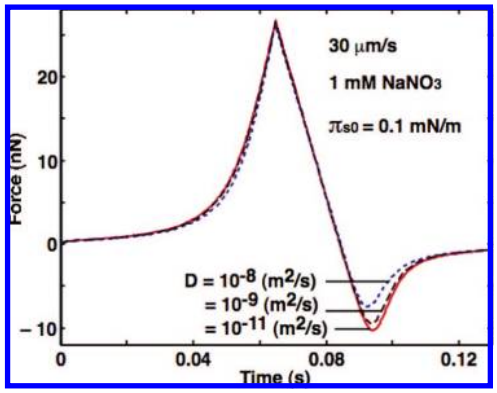

Figure 7. Time variations of the dynamic force $F(t)$ between a bubble and a mica plate in distilled water with 1 mM $NaNO_3$ for the insoluble surface impurities model with different surface diffusion coefficients D. The scan rate is 30 μm/s, the initial magnitude of the surface pressure π_{s0} is 0.1 mN/m, and the initial separation h_{init} is 1.85 μm.

during the approach phase and speeds up the fastest during the retraction phase. In all cases, dh/dt actually exceeds or overshoots the instantaneous scan rate dX/dt toward the end of the retraction phase. This is illustrated explicitly in the plot of the normal surface velocity at the center of the film: $dh(0,t)/dt$ as depicted in Figure 4 for the insoluble surface impurities model.

The behavior of the hydrodynamic pressure $p(r,t)$ (Figure 10), the disjoining pressure $\Pi(r,t)$ (Figure 11), and the total dynamic pressure $(p + \Pi)$ (Figure 12) also reflects the consequences of the different models of surface boundary conditions. During the approach phase from times (a)−(d), the hydrodynamic pressure $p(r,t)$ for the no-slip model (Figure 10a) and insoluble surface impurities model (Figure 10d) is very similar. While the Navier slip model reaches the maximally repulsive hydrodynamics pressure profile within the same time (c) (Figure 10c), this pressure falls away more rapidly at times (d) and (e). However, during the retraction phase, the attractive hydrodynamic pressure $p(r,t)$ profiles are similar for the Navier slip and insoluble surface impurities models while the pressure profile of the no-slip case in the retraction phase is about twice as attractive. These observations simply reflect the higher hydrodynamic drag that arises from the no-slip air/water interface. At all times, the magnitude of the hydrodynamic pressure profile of the full-slip case is, as expected, smaller than that of all other models, and as the numerical result indicate, by a factor of about 4.

Around the force maximum at times (c)−(f), when the film is the thinnest, the magnitude of the disjoining pressure $\Pi(r,t)$ is expected to be large. The full-slip case shows the largest disjoining pressure profiles, particularly at time (c), because this boundary condition results in the lowest hydrodynamic resistance and hence the bubble flattens the most (see Figure 8) with the aqueous film attaining the thinnest minimum value of all models considered here.

Turning now to the total dynamic pressure $(p + \Pi)$ of the different models given in Figure 12, we see that the no-slip model (Figure 12a) and the insoluble surface impurities model (Figure 12d) have almost identical pressure profiles. Thus, from the augmented Young−Laplace equation (eq 1), the film thickness of these two models should also be very similar, as we have seen

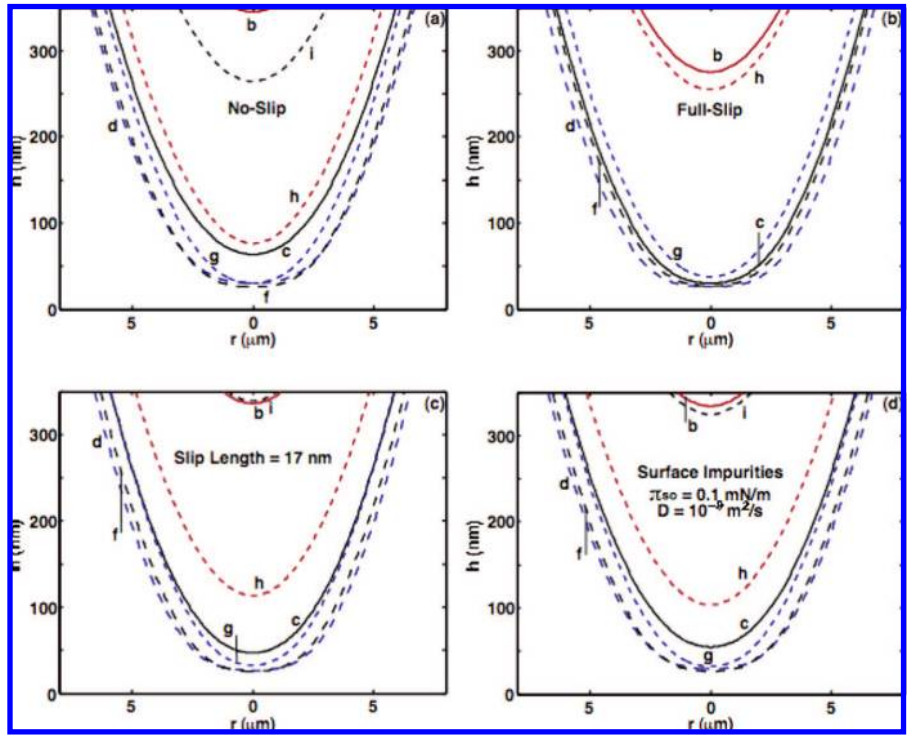

Figure 8. Radial variations of the thickness of the film $h(r,t)$ at some of the key time points indicated on the force curve in Figure 4 corresponding to different boundary conditions at the air/water interface: (a) no-slip, (b) full-slip, (c) Navier slip with a slip length b of 17 nm, and (d) insoluble surface impurities model with a surface diffusion coefficient D of 10^{-9} m^2/s and initial surface pressure π_{s0} of 0.1 mN/m.

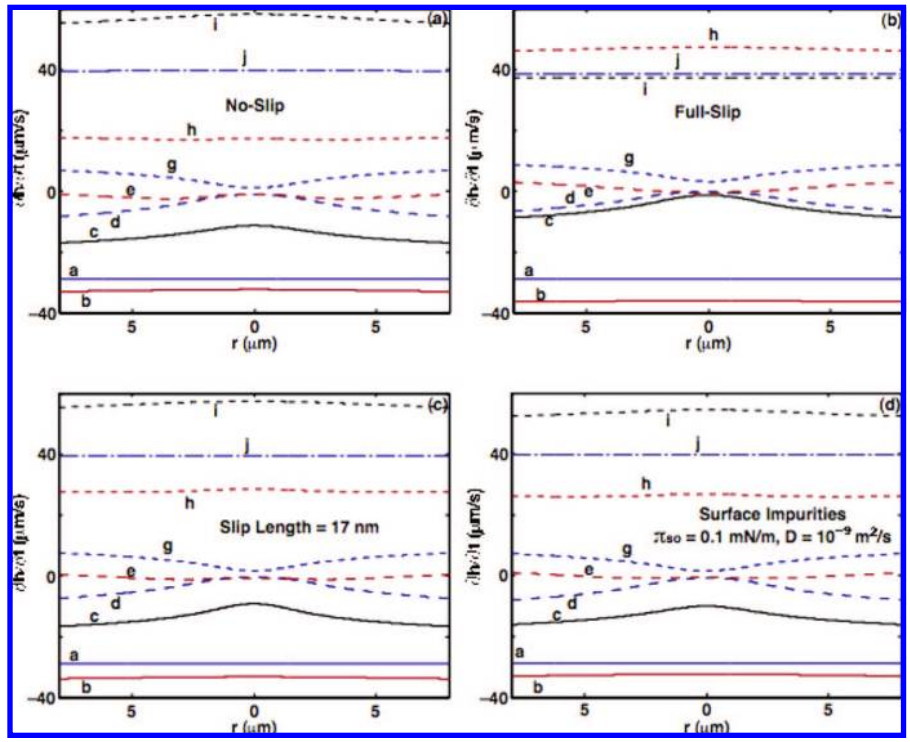

Figure 9. Radial variations of the normal velocity $\partial h(r,t)/\partial t$ of the air/water interface at some of the key time points indicated on the force curve in Figure 4 corresponding to different boundary conditions at the air/water interface: (a) no-slip, (b) full-slip, (c) Navier slip with a slip length b of 17 nm, and (d) insoluble surface impurities model with a surface diffusion coefficient D of 10^{-9} m^2/s and initial surface pressure π_{s0} of 0.1 mN/m.

in Figure 8 for most of the approach−retract cycle. Again, the results for the full-slip model (Figure 12b) differ the most from those of these two models, especially during the time period (c)−(g), with the behavior of Navier slip model (Figure 12c) falling in somewhere in between. Note that, in all cases, the maximum value of the total dynamic pressure ($p + \Pi$) did not exceed the unperturbed Laplace pressure of the bubble: ($2\sigma/R_b$) $\sim$ 2.6 kPa; the curvature of the air/water interface of the bubble did not change sign to form a dimple during the course of the interaction.

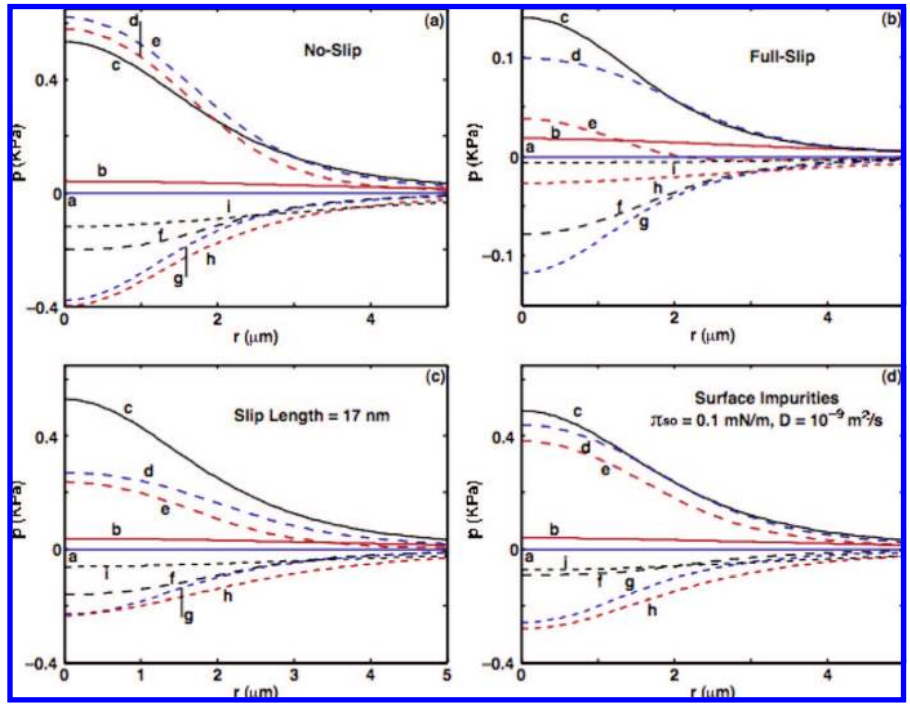

Figure 10. Radial variations of the hydrodynamic pressure p in the film between the bubble and the mica surface at the key time points indicated on the force curve in Figure 4 corresponding to the boundary conditions at the air/water interface: (a) no-slip, (b) full-slip, (c) Navier slip with a slip length b of 17 nm, and (d) insoluble surface impurities model with a surface diffusion coefficient D of 10^{-9} m^2/s and initial surface pressure π_{s0} of 0.1 mN/m.

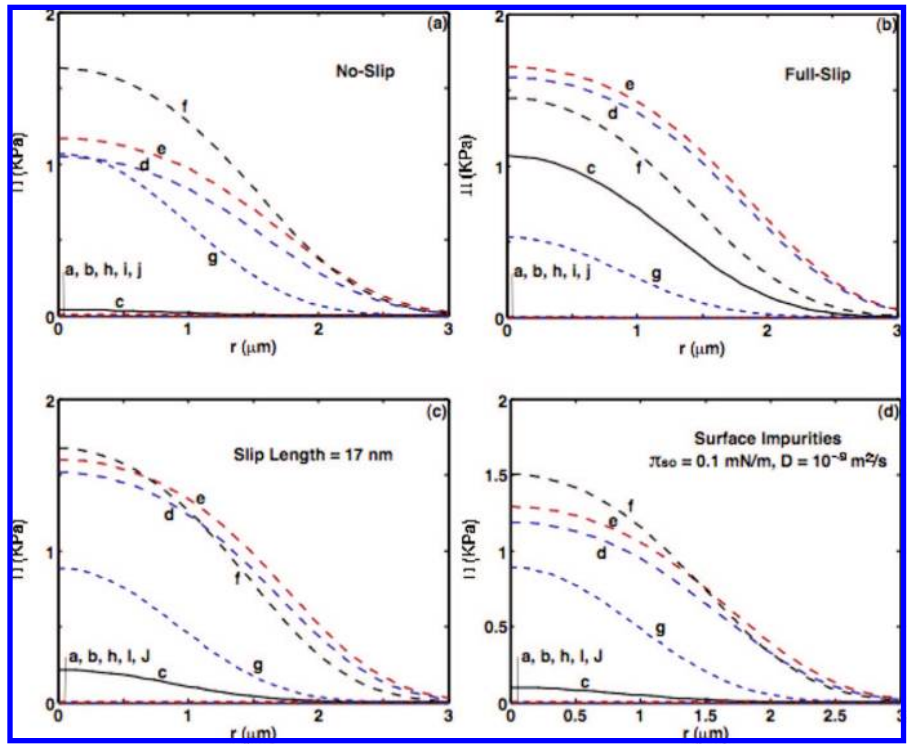

Figure 11. Radial variations of the electrostatic pressure Π in the film between the bubble and the mica surface at key time points indicated on the force curve in Figure 4 corresponding to the boundary conditions at the air/water interface: (a) no-slip, (b) full-slip, (c) Navier slip with a slip length b of 17 nm, and (d) insoluble surface impurities model with a surface diffusion coefficient D of 10^{-9} m^2/s and initial surface pressure π_{s0} of 0.1 mN/m.

In the bubble−mica system, the disjoining pressure Π due to electrical double layer interactions is always repulsive (Figure 13a), so it is interesting to see how this combines with the hydrodynamic pressure p (Figure 13b) to give a zero net force at the time point (g) (see Figure 4) of the retract branch of the force curve. In Figure 13d, we see that at time (g) the total pressure ($p + \Pi$) is repulsive (positive) in the central, small r, portion of the film but is attractive (negative) in the outer, large r, part of the film. A zero net force results from the cancelation between positive and negative areas in the function $[r(p + \Pi)]$

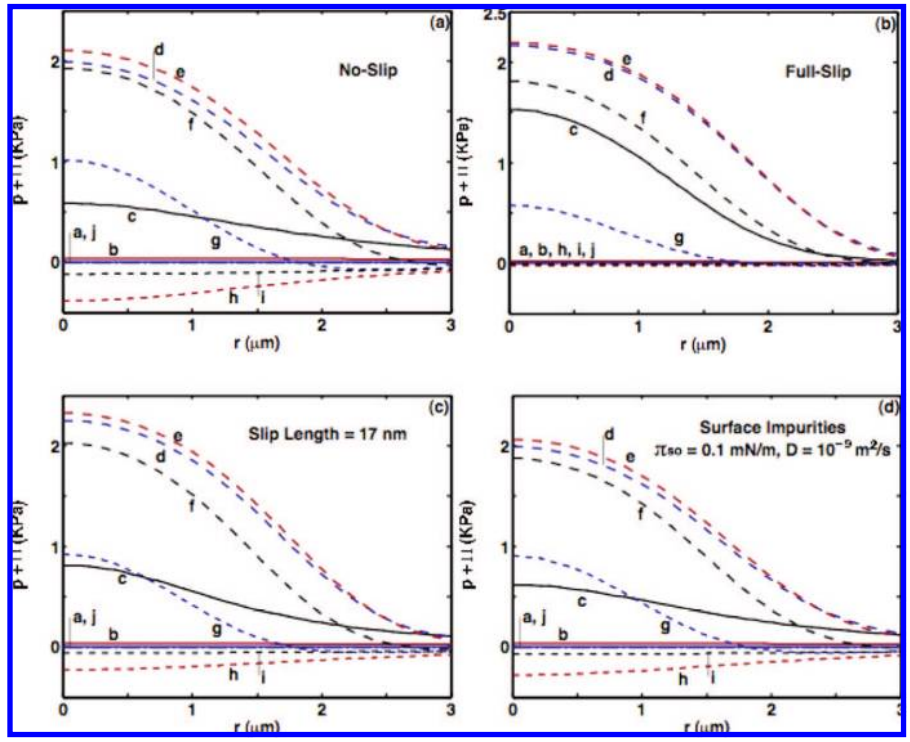

Figure 12. Radial variations of the total dynamic pressure ($p + \Pi$), hydrodynamic pressure (p), and the electrostatic pressure (Π) in the film between the bubble and the mica surface at key time points indicated on the force curve in Figure 4 corresponding to the boundary conditions at the air/water interface: (a) no-slip, (b) full-slip, (c) Navier slip with a slip length b of 17 nm, and (d) insoluble surface impurities model with a surface diffusion coefficient D of 10^{-9} m^2/s and initial surface pressure π_{s0} of 0.1 mN/m. The Laplace pressure of the bubble is 2.6 KPa.

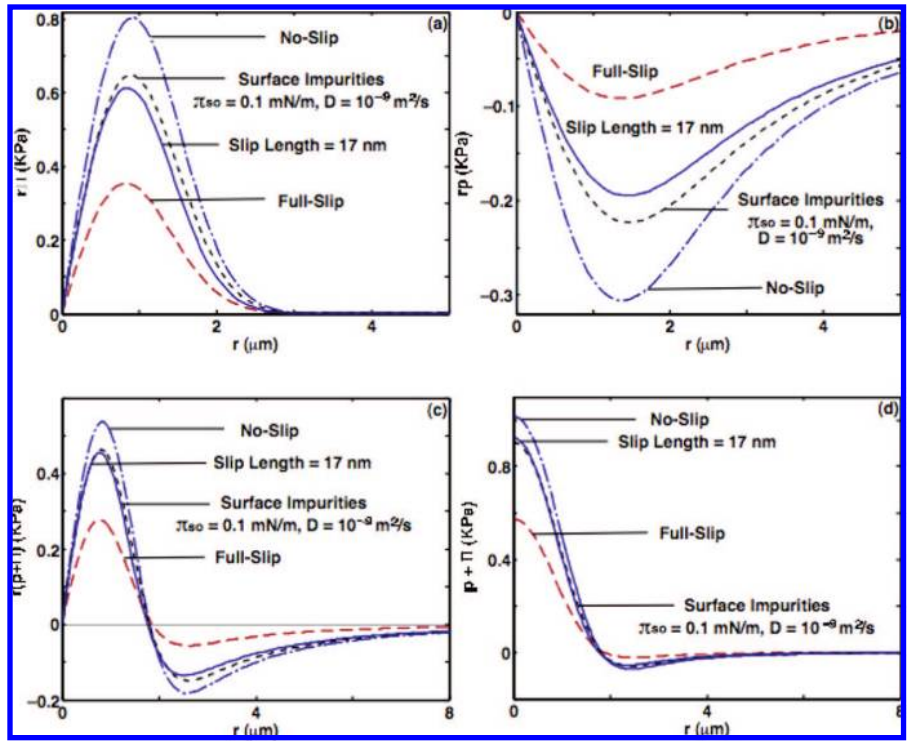

Figure 13. Variation of the hydrodynamic pressure p and disjoining pressure Π at the time point (g), $t = 0.0840$ s in Figure 4, when the force between the bubble and the mica surface $F(t) = 2\pi\int_0^\infty[p(r,t) + \Pi(h(r,t))]r\,dr$ is nearly zero.

(Figure 13c). The magnitudes of the hydrodynamic and disjoining pressure profiles are the largest for the no-slip model and smallest for the full-slip model, while the pressure profiles for Navier slip model and insoluble surface impurities model are similar in magnitude and are intermediate between the extremes of no-slip and full-slip.

Turning now to the surface velocity u_s at the bubble, which for the full-slip model is given by eq 6b, the Navier slip model

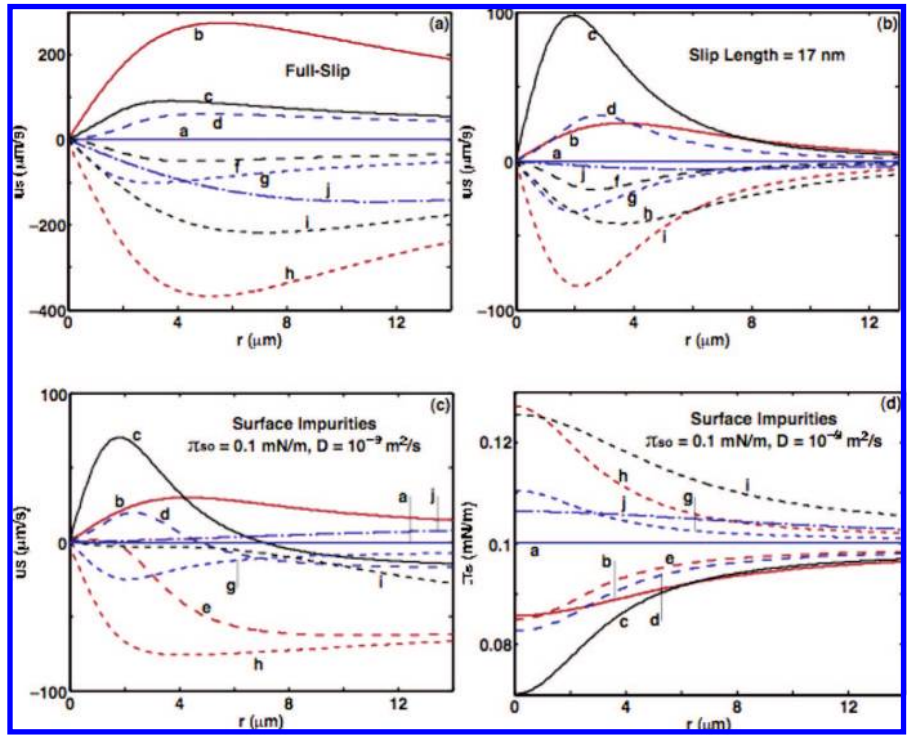

Figure 14. Radial variations of the surface velocity u_s at the air/water interface at key time points indicated on the force curve in Figure 4 corresponding to the boundary conditions at the air/water interface: (a) full-slip, (b) Navier slip with a slip length b of 17 nm, (c) insoluble surface impurities model with a surface diffusion coefficient D of 10^{-9} m^2/s and initial surface pressure π_{s0} of 0.1 mN/m, and (d) the corresponding variations in surface pressure π_s.

by eq 7b, the insoluble surface impurities model by eq 8b while it is zero, by definition, for the no-slip model. From Figure 14a, we see that the surface velocity u_s for the full-slip model is large and positive; that is, surface flow is directed from the center to the edge of the film ($u_s > 0$) as the dynamic force just starts to increase along the approach branch around time (b) in Figure 4. Around the force maximum, we have already seen in Figure 9 that the normal velocity $\partial h(r,t)/\partial t$ of the air/water interface is small and this is also seen in the small magnitudes of the surface velocity at times (c)−(f) in Figure 14a. On the retraction branch of the dynamic force curve, the surface velocity becomes large and negative; that is, surface flow is now directed from the edge of the film toward the center ($u_s < 0$) with the largest magnitude and extent around the time of attractive minimum of the dynamic force.

The expression for surface velocity of the Navier slip model, eq 7b, is similar to the full-slip case, eq 6b, but modulated by the factor $[b/(b+h)]$ which to first order reduces the magnitude and spatial extent of the surface velocity profile (see Figure 14a and b). However, the added hydrodynamic drag at the air/water interface delayed the maximum surface velocity until nearer to time (c).

In addition to having very similar dynamic force curves, the surface velocity for the insoluble surface impurities model, Figure 14c, also appears to be similar to the Navier slip model near the center of the film ($r \leq 4$ μm) but different for large $r \geq 4$ μm. However, this similarity can be misleading, as the behavior of the surface velocity and surface pressure is more complex. The surface velocity of insoluble surface impurities model has an additional contribution from the gradient of the surface pressure, π_s (see eq 8b). During the approach branch, because of the convection−diffusion mechanism of the surface species, one might expect the surface velocity to flow from the center of the film to the edge ($u_s > 0$). This will sweep surfactants out of the film, reduce the surface pressure from the quiescent value, and increase the local interfacial tension. On the other hand, during the retraction phase, one might expect the surface velocity to be directed inward ($u_s < 0$), which will increase the surface pressure π_s above the quiescent value and decrease the local interfacial tension. From Figure 14d, these expectations are indeed fulfilled during the early stages of the approach phase [times (a) to (b)] and during the late stages of the retract phase [times (h)−(j)] and account for around ±20% variation in the surface pressure at different stages of the approach/retract cycle (Figure 14d). However, at other parts of the approach/retract cycle, the behavior of the surface velocity is more complex. For example, at time (c) on the approach curve, the surface velocity is zero at around 7 μm, so that in the central part of the air/water interface, $0 < r < 7$ μm, $u_s > 0$ and the surface velocity is directed outward, but in the outer part of the air/water interface, $r > 7$ μm, $u_s < 0$ and the surface velocity is directed inward, driven by surface diffusion effects. This complex behavior is not present in the Navier slip model in Figure 14b.

Furthermore, we see in Figure 14c that, at time (e) just after the commencement of the retraction phase, the surface velocity is almost entirely directed inward at all parts of the air/water interface ($u_s < 0$), but the surface pressure π_s in Figure 14d remains entirely below the equilibrium value of 0.1 mN/m which implies that there is still a depletion of insoluble surface impurities relative to the equilibrium concentration inside the film. In fact, it is not until time (g) when the dynamic force is around zero before the surface concentration starts to rise above the equilibrium value. Thus, the space and time variations of the surface velocity and surface pressure slightly lag the piezo drive.

The seemingly small variation in surface pressure (±20%) actually has a significant effect on how the surface velocity is

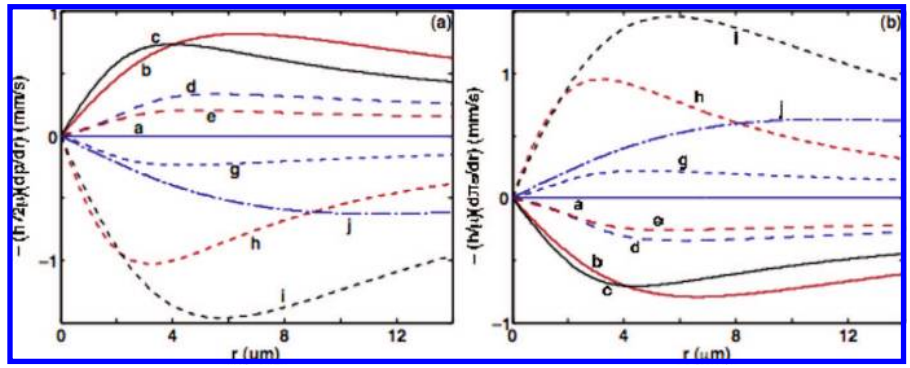

Figure 15. Radial variations of the (a) hydrodynamic pressure, $-(h^2/2\mu)(dp/dr)$, and (b) surface pressure, $-(h/2)(d\pi_s/dr)$, contributions to the tangential surface velocity u_s at the air/water interface at key time points marked in Figure 4 for the insoluble surface impurities model with a surface diffusion coefficient D of 10^{-9} m^2/s and initial surface pressure π_{s0} of 0.1 mN/m.

generated. The surface velocity in the insoluble surface impurities model is given by

$$u_s = -\left(\frac{h^2}{2\mu}\right)\left(\frac{\partial p}{\partial r}\right) - \left(\frac{h}{\mu}\right)\left(\frac{\partial \pi_s}{\partial r}\right) \tag{10}$$

and in Figure 15 we see that numerical cancelation of around two significant figures occurs between the hydrodynamic pressure gradient term and the surface pressure gradient terms that contribute to the surface velocity in Figure 14c. Thus, when the interface contains mobile insoluble impurities, the surface velocity is a very sensitive function of the dynamics of these surface species even though this may not be immediately apparent by comparing the dynamic force between different models. This type of behavior may have important implications for surface rheological effects. Indeed, the surface velocity in the Navier slip model, eq 7b, can be written in a similar form

$$u(z=h, r, t) = u_s = -\left(\frac{h^2}{2\mu}\right)\left(\frac{\partial p}{\partial r}\right) - \left(\frac{-h^2}{2\mu}\right)\left(\frac{h}{h+b}\right)\left(\frac{\partial p}{\partial r}\right) \tag{11}$$

where we formally identify the first term on the right as the full-slip velocity and the second as the correction of the air/water interface deviation from full-slip. However, while eqs 10 and 11 appear similar, the physical contents are quite different.

6. Conclusion

AFM measurements of the dynamic force between a 50 μm radius bubble and a mica surface reveal that, in the presence of SDS above the cmc, the layer of adsorbed surfactant at the air/water interface has rendered it immobile and the no-slip hydrodynamic boundary condition should be used to deduce the dynamic force even at mica−bubble separations close to ∼30 nm.

In the presence of only added salt, 1 mM $NaNO_3$, the hydrodynamic behavior of the air/water interface is intermediate between the no-slip (fully immobile) and full-slip (fully mobile) limits. The dynamic force can be fitted either by the Navier slip model with a fitted slip length of 17 nm or by the insoluble surface impurities model in which we postulate that the presence of a small concentration of mobile surface-active impurities at the air/water interface can alter the hydrodynamic shear stress at the interface. The insoluble surface impurity model offered a plausible quantitative explanation for the fitted slip length required by the Navier slip model to fit experimental data. The different behavior of the surface velocity between the Navier slip model and the insoluble surface impurities model suggests a way to distinguish between these models by suitable further experiments.

Acknowledgment. This work is supported in part by the Australian Research Council (ARC) funding through the Particulate Fluids Processing Centre, a Special Research Centre of the ARC, and through the Australian Minerals Science Research Institute which also receives support from AMIRA international and State Governments of Victoria and South Australia. O.M. is supported by a University of Melbourne Postgraduate Research Scholarship. D.Y.C.C. is a Visiting Professor at the National University of Singapore and an Adjunct Professor at the Institute of High Performance Computing.

Supporting Information Available: Derivation of the generalized Young−Laplace equation, and asymptotic boundary condition for the surface pressure. This material is available free of charge via the Internet at http://pubs.acs.org.

LA802206Q